Extension of A High-Order Petrov-Galerkin Implementation Applied to Non-Radiating and Radar Cross Section Geometries

By

W. Lawton Shoemake

Approved:

W. Kyle Anderson Professor of Computational Engineering (Chair)	Li Wang Research Assistant Professor of Computational Engineering (Committee Member)
Sagar Kapadia Research Assistant Professor of Computational Engineering (Committee Member)	

Extension of A High-Order Petrov-Galerkin Implementation Applied to Non-Radiating and Radar Cross Section Geometries

By

William Lawton Shoemake

A Thesis Submitted to the Faculty of the University
of Tennessee at Chattanooga in Partial
Fulfillment of the Requirements of the
Degree of Master of Science
in Engineering

The University of Tennessee, Chattanooga
Chattanooga, Tennessee

December 2013

ABSTRACT

Capabilities of a high-order Petrov-Galerkin solver are expanded to include N-port systems. Tait-Bryan angles are employed to launch electro-magnetic waves in arbitrary directions allowing off axis ports to be driven. The transverse-electric (TE) formulation is added allowing waveguide geometries to be driven directly. A grid convergence study is performed on a coax-driven waveguide system. Physical data are matched to a hybrid-T junction (magic-T) electromagnetic waveguide structure to verify the TE driving formulation along with the Tait-Bryan angles and modified post-processing routines. A simple sphere case is used to exercise the radar cross section (RCS) routines and to examine the benefits of curving elements for high-order simulations.

DEDICATION

to my family for all their support

ACKNOWLEDGEMENTS

I would like to thank Dr. Anderson, Sagar Kapadia, Li Wang, and Srijith Rajamohan for teaching me the ways of FUNSAFE and Mr. Roberts for letting us play with electricity.

TABLE OF CONTENTS

LIST OF TABLES

LIST OF FIGURES

CHAPTER 1

INTRODUCTION

The most common technique for solving Maxwell's equations using computational methods is the Finite-Difference Time-Domain (FDTD) developed by Yee in 1966 [1]. The FDTD approach greatly limits the discretization of a geometry to rectilinear faces and edges [1, 2]. The development of finite element and finite-volume techniques no longer requires the grid to be rectilinear. Due to the similarity between Maxwell's equations and the compressible Euler equations, finite-volume methods developed for fluid dynamics applications can be readily applied to electromagnetic problems. Similarly finite element methods developed for solving the Euler equations can also be applied to solving Maxwell's equations.

The purpose of this study is to implement and verify capabilities intended to extend the applicability of a high-order streamline upwind Petrov-Galerkin solver previously developed by Anderson et al. [2]. The added capabilities include generalized post processing techniques and a Tait-Bryan rotation routine. The generalized post processing will allow Fourier transform data to be examined for each individual port of a multiport network. This extension is required in order to examine networks consisting of more than a single input and output port which is adequate for a large number of problems involving far-field and non-branching situations but is inadequate for examining the behavior of circuits that have many ports. A power coupler/divider called the hybrid T-junction (magic T) is used to verify this added functionality against measured results. Similarly, the ability to launch an electromagnetic wave in an arbitrary direction is required in order to fully examine the behavior of N-port systems. The solution implemented uses the Tait-Bryan x-y-z convention

of rotations [3]. Here, each port is locally rotated to an be evaluated to determine the data at each location spanning the port. This data is then rotated back where it is used to introduce energy into the field. This approach arguably requires the least and simplest amount of information from the end user to quickly and easily launch a wave in an arbitrary direction. Verification of this code is performed on a coax-waveguide hybrid geometry and a simple waveguide geometry.

Effects of spatial refinement and order of accuracy are examined on the coax-waveguide circuit, for which experimental data is available for comparison, using a sequence of grids with systematic increases in grid density. Lastly the benefits of projecting high-order elements to properly represent the geometry are demonstrated by determining the radar cross section of a perfect electrically conducting (PEC) sphere for which the exact solution is available.

Case Background

Hybrid T-Junction

Microwave circuitry uses hollow-tube waveguides in high power applications. T-junctions operate as power couplers and dividers and depending on which port a signal is applied, the T-junctions will behave as a coupler or divider. The T-junctions are grouped according to which plane the T is in, either the E-plane or H-plane. The hybrid T-junction (magic T) is a combination of the E-plane and H-plane T-junctions. It is an interesting example as it analytically has very useful properties. Driving the co-linear ports will simultaneously sum and difference the inputs.

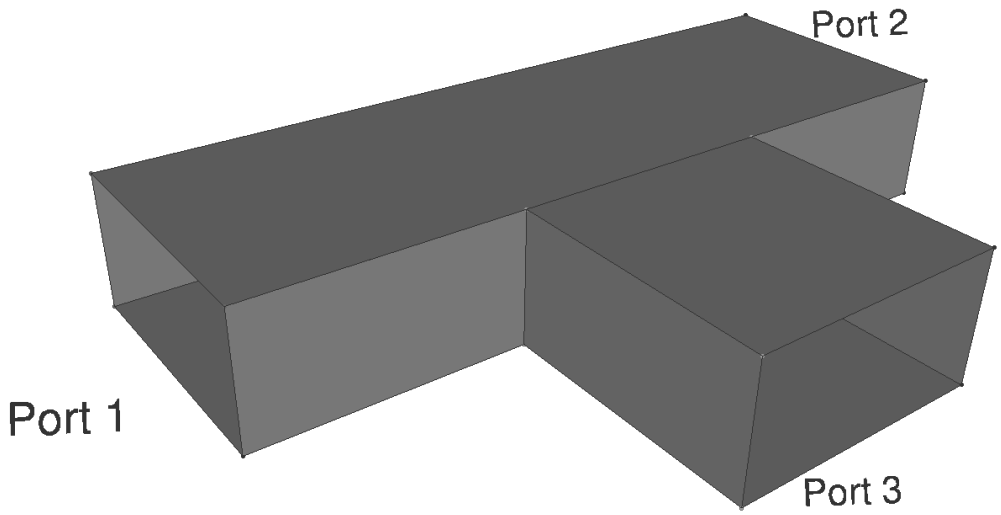

Figure 1.1 H-plane T-junction

Figure 1.1 depicts three inputs to the H-plane T-junction. In the figure the ports are labeled 1, 2, and 3. More descriptive names are the 'H-plane' port for 3, and the other two are the co-linear ports. Power input through port 1 will result in the power being divided between ports 2 and 3. Power input sumultaneously through ports 1 and 2 will result in the sum of these exiting port 3. Therefore if the inputs to port 1 and 2 are in-phase then the power output from port 3 will be the sum of the inputs to ports 1 and 2, whereas if the input to port 1 and 2 are 180° out of phase then the inputs to ports 1 and 2 will cancel and port 3 will have no output. These T-junctions are symmetric about the H-plane port which implies that the behavior of driving one co-linear port will mirror driving the other. Similar to the H-plane T-junction, the E-plane T-junction, shown in figure 1.2, also divides or couples input power depending on the port and phase of the input signal being applied. However, a signal applied to the E-plane port will be divided between the two colinear ports but the output from the colinear ports will be 180° out of phase.

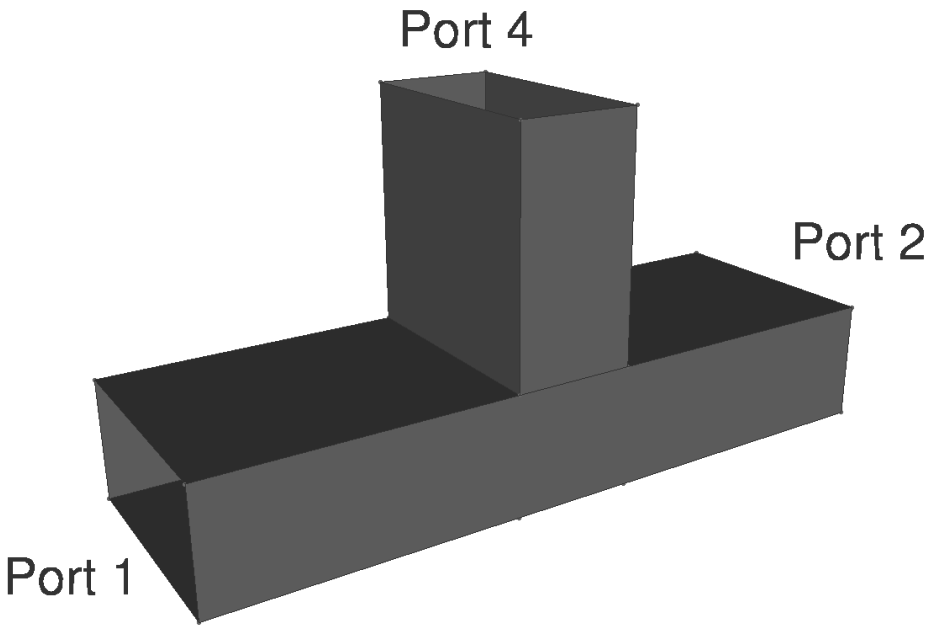

Figure 1.2 E-plane T-junction

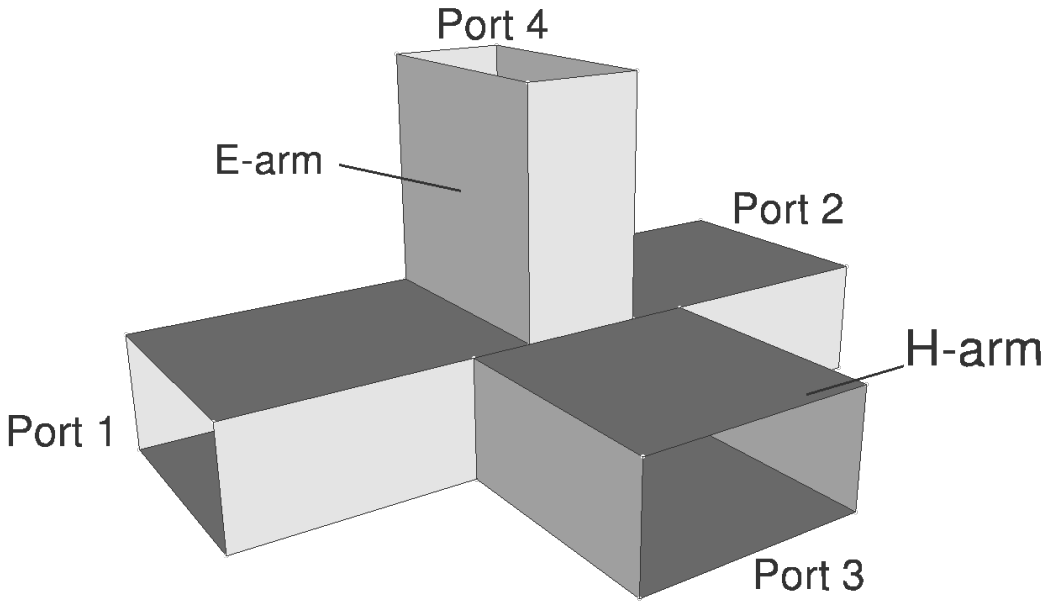

Figure 1.3 Hybrid T-junction (magic-T)

In the case of the magic T, shown in figure 1.3, the T-structure occurs in both planes which combines qualities of the E and H-plane junctions and puts them in the family of

180° hybrid couplers. Hybrid couplers are used to split, combine, or isolate power. In high power applications, this often allows components to be isolated from one another to prevent damage in case of malfunctioning components. In the case of the magic T, power input to port 1 or 2 will produce output from ports 3 and 4; input to port 3 will produce an in-phase output signal from ports 1 and 2 and input to port 4 will produce a 180° out of phase signal from ports 1 and 2. Port 3 is referred to as the summation port and port 4 as the difference port due to their behavior when input signals are applied to both ports 1 and 2. An in-phase signal to ports 1 and 2 will sum at port three and difference at port 4. Port 4 will be isolated should the amplitudes of ports 1 and 2 be the same due to the difference being zero. Similarly port 3 will be isolated if the input signals to ports 1 and 2 are 180° out of phase and of equal amplitude due to the sum being zero.

Coax-Waveguide Hybrid

As seen in figure 1.4, coax cables are comprised of an inner conductor and a braided outer conductor separated by a dielectric. Energy is propagated in electromagnetic waves within the dielectric between the two conductors. The coax-waveguide hybrid system is the same geometry used in [2] for validation and is shown in figure 1.4. The input transverse electromagnetic (TEM) wave propagates through the dielectric in the coaxial cable, transitions into a WR-90 waveguide as a transverse electric (TE) wave, and is transmitted by the coaxial cable at the opposite end of the geometry. To simulate the dielectric, the permittivity in portions of the grid associated with the coaxial cable is set to 2.1, which is the dielectric constant of Polytetrafluoroethylene. This case is used to verify that the material interfaces in the solver [2] are handled properly. This geometry has been examined experimentally and measured data is available for comparison.

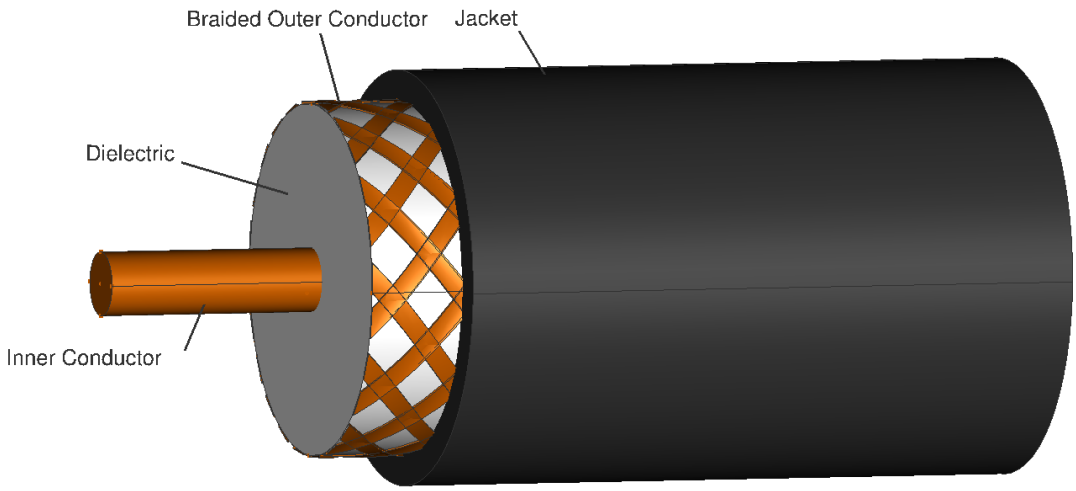

Figure 1.4 Cutaway of a coaxial cable

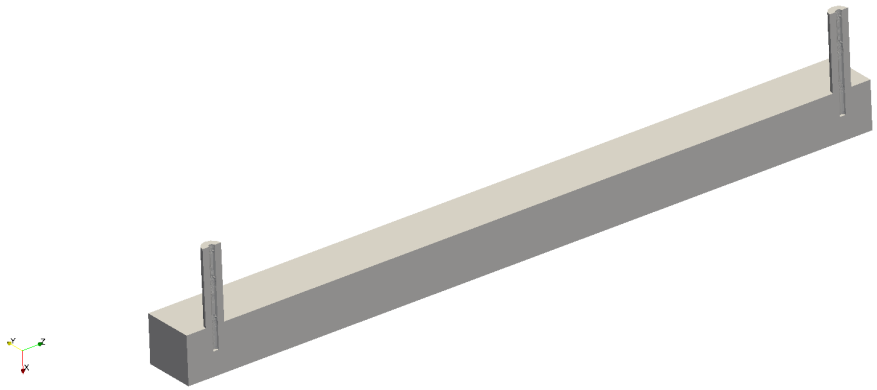

Figure 1.5 Cutaway of the coax-waveguide hybrid geometry

Radar Cross Section of a Sphere

The radar cross section (RCS) relates to the ability of an object to reflect radar in the direction of a receiver. RCS data for an aircraft is difficult to analytically produce, which is why most RCS profiles are obtained from the measured data [4]. Analytic solutions for radar cross sections can be obtained for a limited number of shapes, although the determination

for general objects is usually obtained from experiments or by using numerical techniques [4]. This information allows an object at a distance to be identified with reasonable confidence. While the most common application of RCS is the identification of objects at a distance, such as aircraft and ships, the medical field has found that tumors can be identified non-invasively using microwave radiation and measuring the RCS using similar technology [5, 4]. Here, motivation for developing microwave radar cross section technology stems from the inaccuracy and harmful side effects of other techniques.

Formally in [6] the radar cross section is defined as

$$\sigma = \lim_{r \to \infty} 4\pi r^2 \frac{S_i}{S_s} \tag{1.1}$$

where r is the distance to the object being detected, S_i is the power density incident on the object and S_s is the power density scattered to a receiver. When the receiver is at or close to the location of the transmitter, the radar cross section is referred to as back scatter or the monostatic RCS. When the transmitter and receiver are in two different locations it is referred to as the bistatic RCS [6]. Because an exact solution exists for the bistatic RCS of a sphere [6], a perfectly electric conducting sphere will be used to examine the accuracy of the finite element method described in [2] when applied to this problem.

CHAPTER 2

FULLY UNSTRUCTURED ADAPTIVE FINITE ELEMENTS

Finite Element Method (FEM)

Similar to many other methods, the finite element method approximates a domain by splitting it into an appropriate collection of sub-domains. A governing equation, or set of governing equations, can then be discretized over the simpler sub-domains. The sub-domains can then be reassembled and the full system can be solved. The FEM assumes that the solution variables can be approximated by a linear combination of polynomials within an element [7]. Distinctions between finite element methods arise depending on how the residual is weighted and minimized, and how the interpolation functions are formed. The solver examined in this work is a Petrov-Galerkin approach described in references [2, 8], in which a complete description of the spatial and temporal discretizations are given. It should be noted that Silver-Muller boundary conditions [9] are used at the end of coaxial cables, whereas Perfectly-Matched Layers (PML) [10] are utilized at outer boundaries where locally the waves are not transverse.

Governing Equations

The governing equations in the electromagnetic problems being considered are Maxwell's equations [11].

$$\nabla \times \mathbf{E} = -\frac{\partial \mathbf{B}}{\partial t} \tag{2.1}$$

$$\nabla \times \mathbf{H} = \frac{\partial \mathbf{D}}{\partial t} \tag{2.2}$$

$$\mathbf{D} = \varepsilon \mathbf{E} \tag{2.3}$$

$$\mathbf{B} = \mu \mathbf{H} \tag{2.4}$$

where $\mathbf{E}$ is the electric field, $\mathbf{H}$ is the magnetic field, $\mathbf{B}$ is the magnetic flux density, $\mathbf{D}$ is the electric flux density, ε is the permittivity, and μ is the permeability.

CHAPTER 3

EXTENSION OF CAPABILITES

Generalized Post Processing

A scattering matrix is a framework for organizing the behavior of a multiport network, specifically how the input relates to the output of the system. The matrix is filled by systematically applying a known input to a single port, measuring the output, and storing the ratio of the output to the input in the matrix, i.e. the $S_{1,1}$ entry is a ratio of the power leaving port 1 to the power entering port 1 while the input of every other port is zero. Similarly, the $S_{1,2}$ entry is the ratio of the power leaving port 1 to the power entering port 2 while the input of every other port is zero [11]. These definitions are given in equations 3.1 and 3.2.

$$S_{i,j} = \frac{P_i^{out}}{P_j^{in}}\bigg|_{P_k^{in}=0\,\forall\, k\neq j} \tag{3.1}$$

$$\begin{bmatrix} P_1^{out} \\ \vdots \\ P_i^{out} \\ \vdots \\ P_N^{out} \end{bmatrix} = \begin{bmatrix} S_{1,1} & \dots & S_{1,j} & \dots & S_{1,N} \\ \vdots & & \vdots & & \vdots \\ S_{i,1} & \dots & S_{i,j} & \dots & S_{i,N} \\ \vdots & & \vdots & & \vdots \\ S_{N,1} & \dots & S_{N,j} & \dots & S_{N,N} \end{bmatrix} \begin{bmatrix} P_1^{in} \\ \vdots \\ P_j^{in} \\ \vdots \\ P_N^{in} \end{bmatrix} \tag{3.2}$$

To determine the scattering parameters at each port over a wide range of frequencies a Gaussian pulse is used that contains sufficient energy over the desired frequency range. Discrete Fourier transforms are dynamically accumulated at each port throughout the time evolution of the simulation. Note that an individually driven port can be used to obtain each column of the scattering matrix. To assemble the scattering matrix of the magic T, the capabilities of the solver (described in reference [2]) to assemble scattering matrices had to be extended from only supporting two port networks to supporting N-port networks. Furthermore the scattering matrix for the magic T is symmetric [11].

Figure 3.1 shows the comparison between the experimental results available in [12] and the simulated data. The mesh used to obtain data shown in figure 3.1 contains approximately 16,000 nodes with approximately 12,800 nodes in the magic T and 4,200 nodes in the PML regions at the end of each port. However, quadratic elements were used resulting in 120,815 degrees of freedom. For these results, a sine wave is used at each frequency rather than utilizing the Gaussian pulse. Here each simulation is run until the incident wave is transmitted to and becomes becomes periodic over every port. A Fourier transform is then computed using data obtained from the immediately following period.

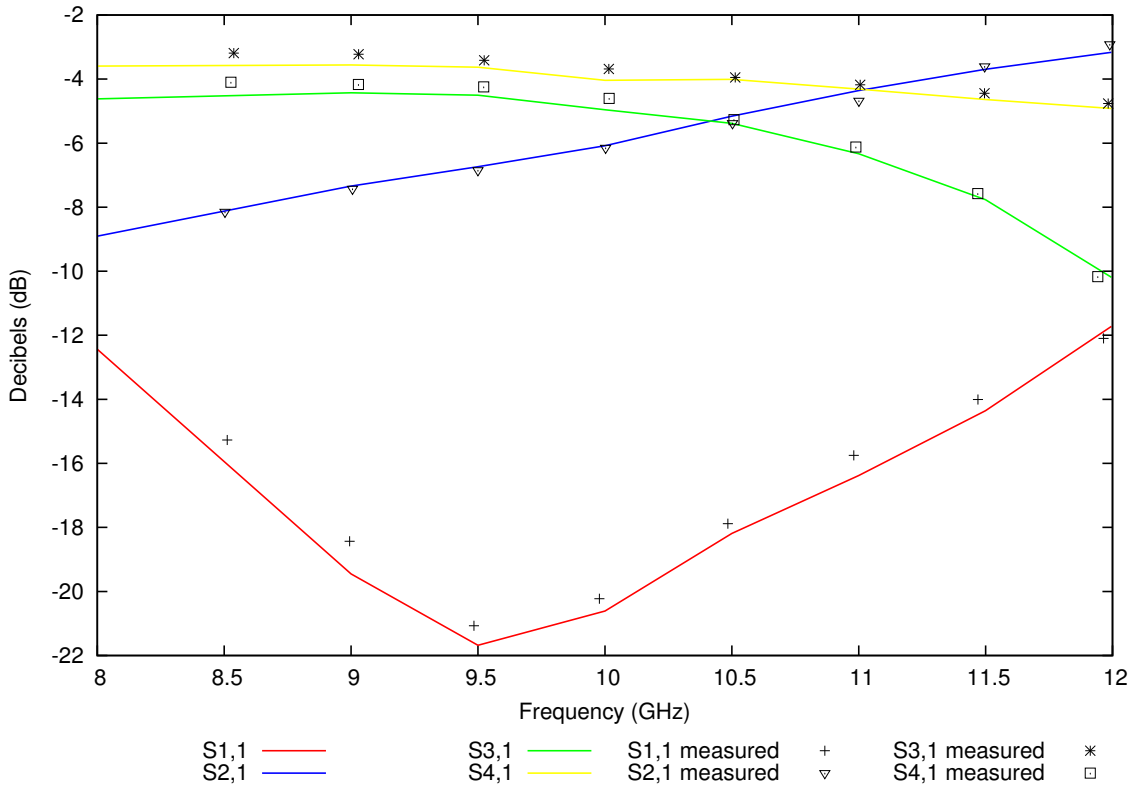

Figure 3.1 Simulated scattering parameters compared to experimental data for the magic T

Figure 3.1 shows good agreement between the experimental and simulated results for each port across the range of frequencies examined and demonstrates that the extensions for computing N-port scattering parameters work properly.

Implementation of Tait-Bryan Angles

To form the full scattering matrix shown in equation 3.2, each port of the network has to be driven individually while the other ports are held passive. In the code described in reference [2], each port is assumed to align along a coordinate axis. With such a rigid assumption, the input of energy along a non-aligned axis would require the mesh to be rotated for every off-axis port. Though this is not a very elegant or robust method, it

is easy to implement. However, should the simulation of interest require two ports to be simultaneously driven, the mesh rotation method is no longer sufficient. The addition of Tait-Bryan rotations [3] enables each port to be driven along arbitrary directions, thereby extending the applicability of the solver to many other geometries.

The Tait-Bryan x-convention of rotations was chosen due to all rotations being extrinsic around the X, Y, and Z axes. The author saw this convention as the most intuitive as the second and third rotations are not dependent on any of the intrinsic axes. This can be seen in the rotation matrices [3],

$$\mathbf{R}_x(\alpha) = \begin{pmatrix} 1 & 0 & 0 \\ 0 & cos(\alpha) & \text{-}sin(\alpha) \\ 0 & sin(\alpha) & cos(\alpha) \end{pmatrix} \tag{3.3}$$

$$\mathbf{R}_y(\beta) = \begin{pmatrix} cos(\beta) & 0 & sin(\beta) \\ 0 & 1 & 0 \\ \text{-}sin(\beta) & 0 & cos(\beta) \end{pmatrix} \tag{3.4}$$

$$\mathbf{R}_z(\gamma) = \begin{pmatrix} cos(\gamma) & \text{-}sin(\gamma) & 0 \\ sin(\gamma) & cos(\gamma) & 0 \\ 0 & 0 & 1 \end{pmatrix} \tag{3.5}$$

where α, β, γ are the rotations around the extrinsic X, Y, and Z axes respectively. Let $\mathbf{V}$ be a vector of the coordinates of a point at the original orientation of a port and $\mathbf{V}'$ be a vector of the coordinates of a point at the ideal orientation of the same port. Then

$$\mathbf{V}' = \mathbf{R}_z(\gamma)\mathbf{R}_y(\beta)\mathbf{R}_x(\alpha)\mathbf{V} \tag{3.6}$$

$$\mathbf{V} = \mathbf{R}_x^{\text{-}1}(\alpha)\mathbf{R}_y^{\text{-}1}(\beta)\mathbf{R}_z^{\text{-}1}(\gamma)\mathbf{V}'. \tag{3.7}$$

Figures 3.2 - 3.5 will illustrate an example. Suppose we have a port at the orientation shown in figure 3.2 and a canonical formulation for a wave propagating in the positive Z direction as shown in figure 3.5. Note that the rotations required to align the port with the canonical driving formulation are known from the geometry of the problem. First the domain is rotated -15° about the X axis so that the vector shown in figure 3.2 will lie in the X-Z plane, the results of which are shown in figure 3.3. Subsequently a -30° rotation about the Y axis is then made so that the vector will align along the positive Z axis as shown in figure 3.4. Lastly, a rotation of -45° will put the domain depicted in the X-Y plane with the surface normal pointing in the positive Z direction. Thus the port is oriented such that the canonical formulation can easily be evaluated on coordinates $V^{'}$.

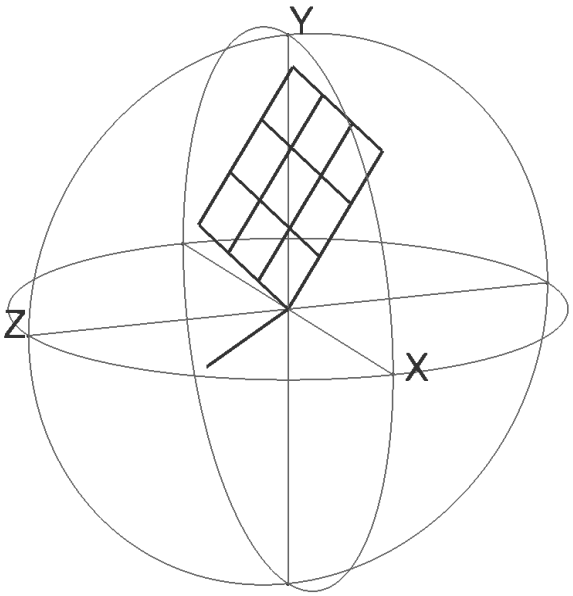

Figure 3.2 Initial orientation of the port

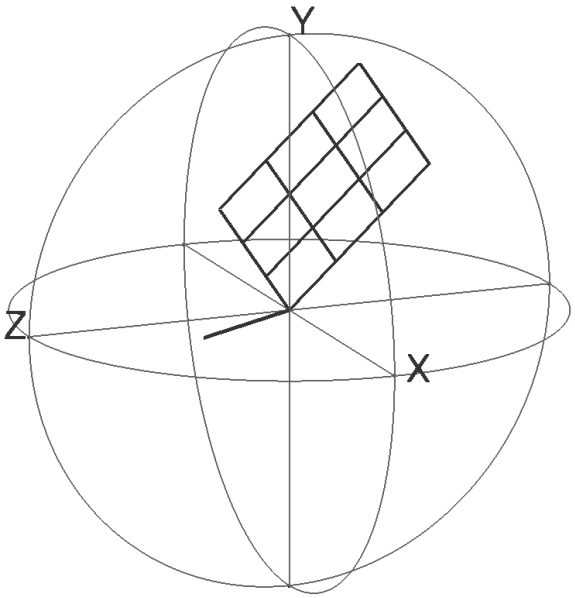

Figure 3.3 A rotation of -15° about the X axis has been performed from figure 3.2

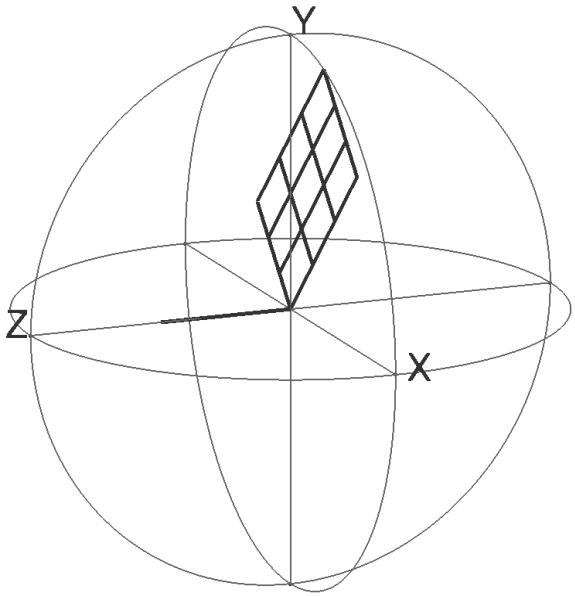

Figure 3.4 A rotation of -30° about the Y axis has been performed from figure 3.3

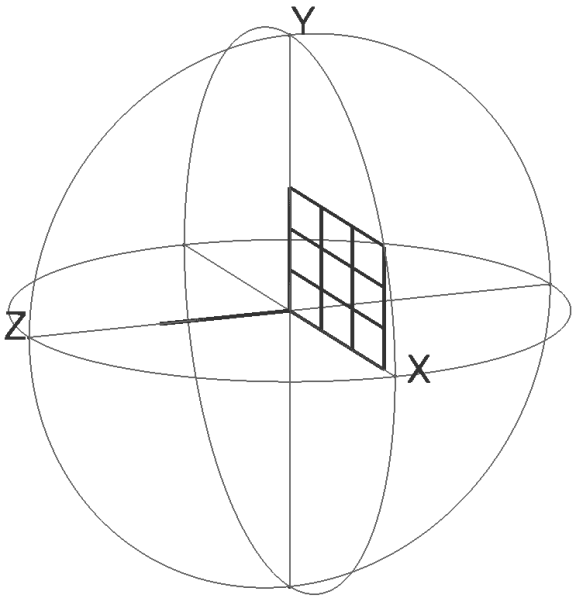

Figure 3.5 A rotation of -45° about the Z axis has been performed from figure 3.4

From this example it is seen that a coordinate at the original port location can be rotated such that it lies at the ideal location for the canonical formulation. Once the Q values, comprised of the field variables **D** and **B**, have been set by the formulation, the Q values, not the coordinates, need to be rotated back to the original orientation of the port. Using equation 3.7 and substituting the Q values for $V^{'}$ the Q values needed at the original port orientation can be found.

The rotations are applied in the solver immediately prior to computing the Q values at the Gauss points on the surface of a port. The coordinates of a Gauss point are rotated to align with the driving formulation, the driving formulation is computed, and the Q values are rotated back to the original orientation. These Q values are then used in computing the flux along the face of the port to be used in the Riemann solver.

Transverse Electric Formulation

The three primary classifications of electromagnetic waves are transverse electromagnetic (TEM), transverse electric (TE), and transverse magnetic (TM). The names accurately describe the wave characteristics in relation to the direction the wave is propagating. The transverse electromagnetic wave only has electric or magnetic components perpendicular to the direction of propagation. Similarly TE waves have magnetic components in the direction of propagation and electric components are perpendicular, whereas TM waves have electric components in the direction of propagation and the magnetic components are perpendicular. TEM waves will not propagate through a hollow waveguide, therefore a TE or TM formulation is needed for these simulations. Prior to the current work the only method available in the code for driving rectangular waveguides were via a coaxial cable. This requires geometry that is not of interest and produces unwanted reflections. Hence the TE and TM formulations are needed for accurately simulating hollow-tube waveguides. The formulations implemented in the solver have been taken from Balanis [6], which are given in a generalized form appropriate for multiple modes.

$$E_x^+ = A_{m,n}\frac{\beta_y}{\varepsilon}cos(\beta_x x)sin(\beta_y y)e^{-j\beta_z z} \tag{3.8}$$

$$E_y^+ = -A_{m,n}\frac{\beta_x}{\varepsilon}sin(\beta_x x)cos(\beta_y y)e^{-j\beta_z z} \tag{3.9}$$

$$E_z^+ = 0 \tag{3.10}$$

$$H_x^+ = A_{m,n}\frac{\beta_x\beta_z}{\varepsilon}sin(\beta_x x)cos(\beta_y y)e^{-j\beta_z z} \tag{3.11}$$

$$H_y^+ = A_{m,n}\frac{\beta_y\beta_z}{\varepsilon}cos(\beta_x x)sin(\beta_y y)e^{-j\beta_z z} \tag{3.12}$$

$$H_z^+ = -jA_{m,n}\frac{\beta_c^2}{\varepsilon}cos(\beta_x x)cos(\beta_y y)e^{-j\beta_z z} \tag{3.13}$$

In equations 3.8 - 3.13, $A_{m,n}$ is an arbirary amplitude, m and n are mode numbers, a is the width of the waveguide, b is the height of the waveguide and β is the wave number and

$$\beta^2 = \omega^2\mu\varepsilon = \beta_x^2 + \beta_y^2 + \beta_z^2$$
$$\beta_x = \frac{m\pi}{a}$$
$$\beta_y = \frac{n\pi}{b}$$
$$\beta_z^2 = \beta^2 - \beta_c^2$$
$$\beta_c^2 = \beta_x^2 + \beta_y^2.$$

Different field configurations exist for combinations of m and n. $TE_{1,0}$ however, is the dominant mode and has the lowest cutoff frequency [11]. This $TE_{1,0}$ formulation has been used to drive the hybrid T-junction mentioned earlier in chapter 3.

CHAPTER 4
VERIFICATIONS

Three cases have been examined for the simulated solutions that could be compared with either measured or analytical data. The hybrid T-junction presented earlier has been used to verify the TE formulation and the generalized scattering parameters. To verify that the Tait-Bryan angle implementation is correct, the coax-waveguide hybrid is rotated into several different orientations and the solutions are compared to that of an unrotated geometry to verify that the solutions are unchanged by rotation. A grid convergence study is also conducted to examine the effects of mesh refinement and the order of accuracy. In a final test case, the radar cross section of a perfect electrically conducting sphere is computed and compared to the analytical solution to study the effects on the solution caused by representing the geometry as a linear surface.

Tait-Bryan Angle Implementation

Verification of the Tait-Bryan angle implementation is performed on the hybrid coax-waveguide system shown previously in figure 1.5. Here, the waveguide is rotated around each axis and the solution is compared to that of the unrotated geometry to verify that the solution is the same in each case. A 30 ° rotation around each axis is used to verify that each portion of the rotation matrices are correct. A final case is run by combining a 15 ° rotation around the X-axis, 30 ° rotation about the Y-axis, and 45 ° rotation around the Z-axis. A depiction of each case can be seen in figures 4.1-4.5. For each of these cases the driving port

is also rotated in order to properly simulate the system. The mesh used has 13,000 nodes sothat using quadratic elements result in a total of 89,476 degrees of freedom. Note that this grid is used only to verify the correct implementation of the Tait-Bryan angles and is not necessarily representative of the level of refinement required to obtain a grid-converged solution.

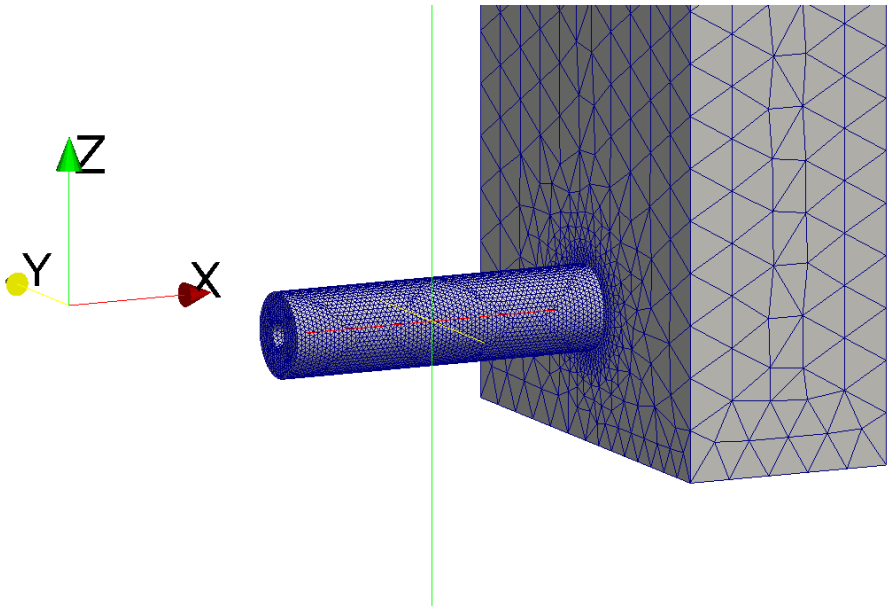

Figure 4.1 The computational mesh shows the input coaxial cable before any rotations; Without any rotations applied the driving port and driving formulation are aligned with the X axis.

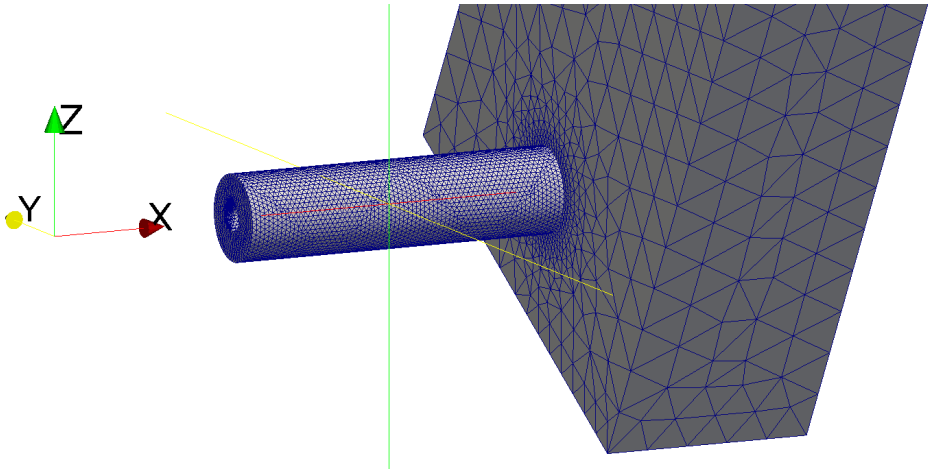

Figure 4.2 The mesh has been rotated 30 ° around the X-axis therefore the orientation of the driving formulation must also be rotated. The positive X-axis is into the page.

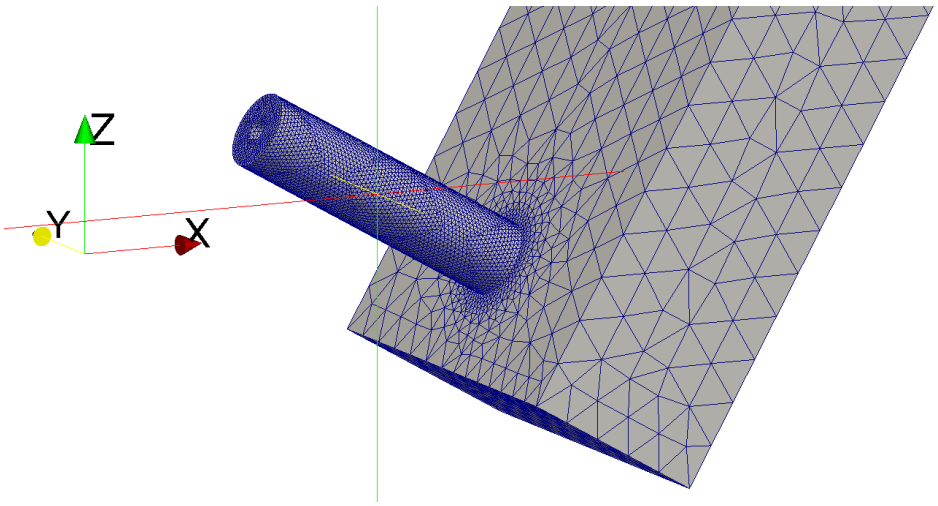

Figure 4.3 The mesh has been rotated 30° around the Y-axis. The positive Y-axis projects out of the page.

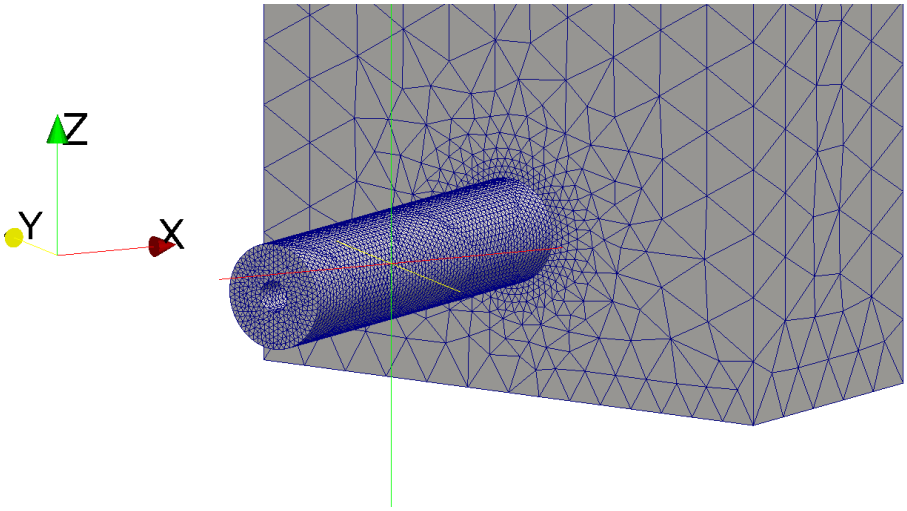

Figure 4.4 The mesh has been rotated 30° around the Z-axis.

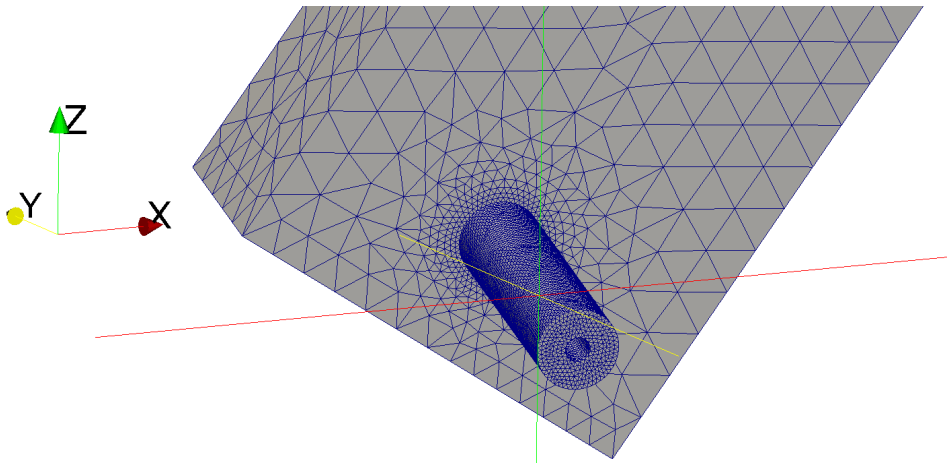

Figure 4.5 The mesh has been rotated 45° around the Z-axis, 30° around the Y-axis, 15° around the X-axis .

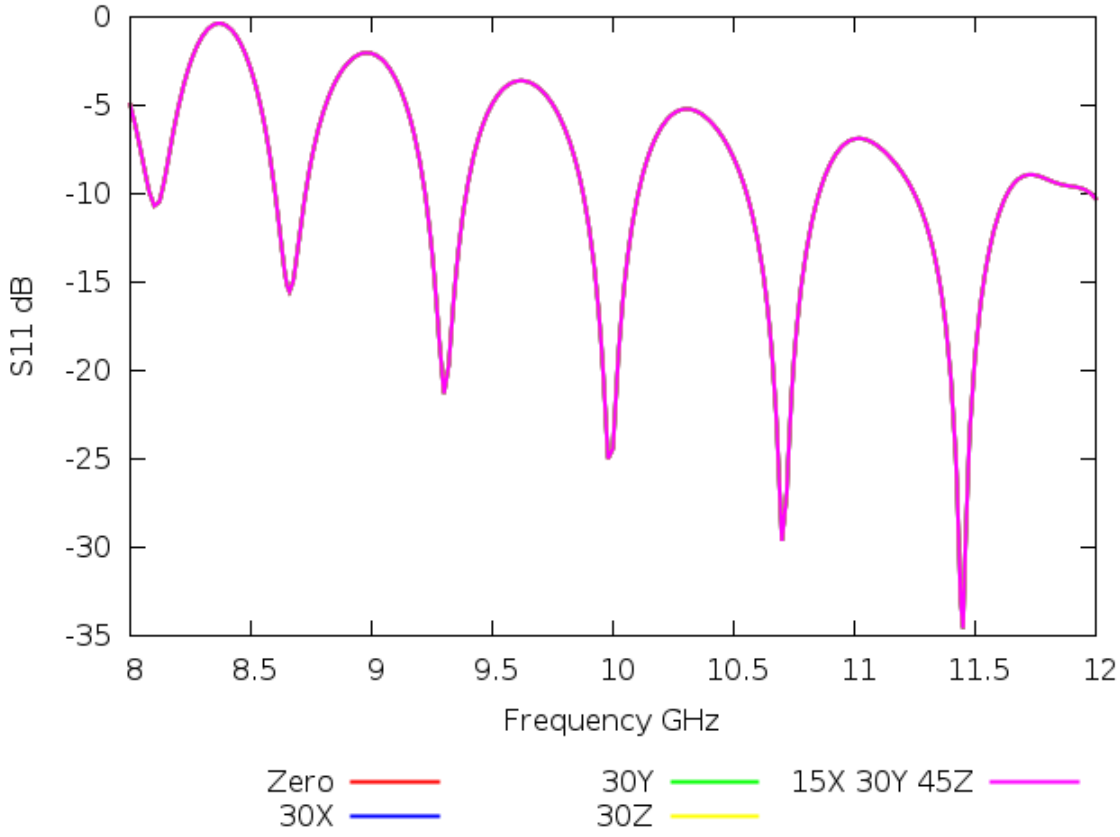

Figure 4.6 Scattering parameters of the geometry with a 45° rotation around the Z-axis, 30° rotation around the Y-axis, 15° rotation around the X-axis

As figure 4.6 shows, the resulting scattering parameters are unaffected by the orientation of the mesh as expected.

Grid Convergence Studies for the Coax-Waveguide Hybrid

Grid convergence studies have been performed on the coax-waveguide system to examine the level of refinement necessary to obtain accurate results and to compare the relative efficiency of linear and quadratic elements. A transverse electromagnetic (TEM) wave is applied to one of the cables, which subsequently transfers the energy into the waveguide. The transition into the waveguide immediately reflects part of the incident wave back into the originating coax cable. The remaining portion of the incident wave traverses the waveguide as a transverse electric (TE) wave. At the opposite end of the waveguide, the TE wave is either absorbed into the output coaxial cable or is reflected back through the waveguide.

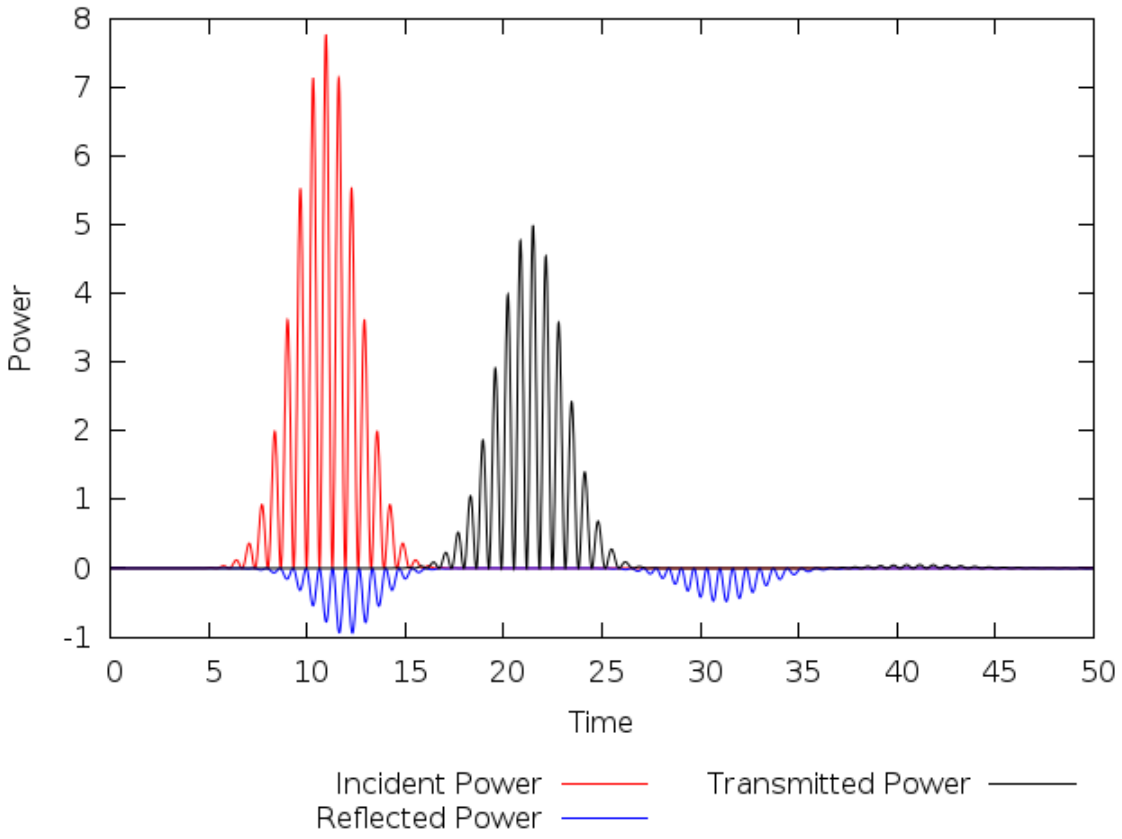

Figure 4.7 Incident, reflected, and transmitted power over time

Figure 4.7 shows the time variation of power at each port. Reflected power is evident shortly after the incident power appears, which is an indication of power transitioning into the waveguide. Reflected power also appears at a later time, which indicates reflections from the opposite end of the waveguide. Similarly, the transmitted power is also apparent in the figure. During the simulation, Fourier transforms of the power are accumulated and are subsequently compared to experimental data [13] in the form of scattering parameters.

Node spacing greatly impacts the accuracy of simulations involving wave propagation. This is due to the Nyquist-Shannon sampling theorem [14] which states that the lowest possible sampling frequency for reconstructing the original signal is twice the original frequency. The sampling frequency directly corresponds to a sampling wavelength which then determines the minimum spacing in the mesh. The minimum spacing must be applied

to the entire mesh, not just the regions of interest. Should the mesh spacing exceed that determined by the sampling theorem, the solution will deteriorate [14].

Mesh refinement (also known as H-refinement) refers to the spacing between the nodes in the mesh, whereas order refinement (P-refinement) refers to the polynomial order of the shape functions. H-refinement usually refers to spatially refining the elements while holding the order of accuracy fixed. Conversely, P-refinement sequentially increases the order of polynomials representing the solution within each element.

Solutions have been obtained on each grid using both P1 and P2 elements. Table 4.1 shows the degrees of freedom for eight sequentially refined meshes. A depiction of one mesh in the vicinity of a coaxial cable is shown in figure 4.8.

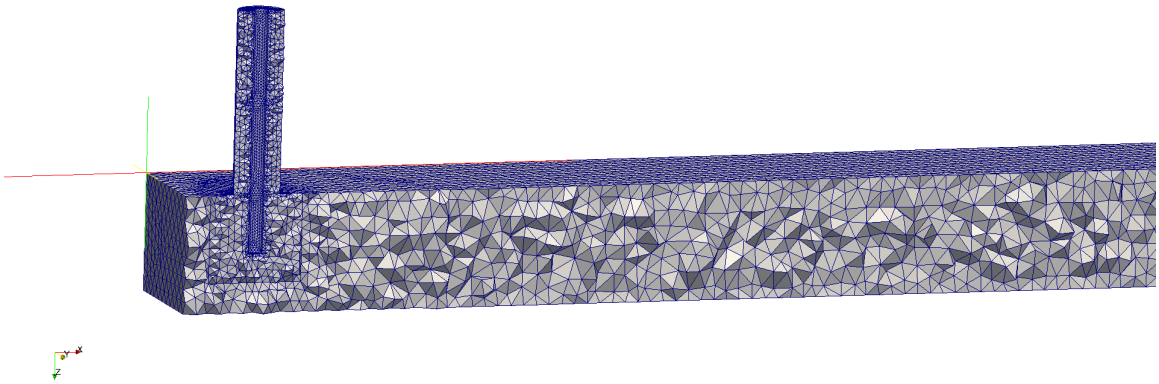

Figure 4.8 The inner conductor of the coax can be seen protruding into the waveguide and the resolution surrounding the coax to waveguide transition

Table 4.1 Degrees of freedom associated with test meshes; an 'X' beside an entry indicates that a simulation was not run

	P1	P2
mesh 1	X 831	5,646
mesh 2	X 1,889	13,177
mesh 3	3,965	28,177
mesh 4	6,686	48,409
mesh 5	13,000	89,476
mesh 6	40,000	300,000
mesh 7	100,00	X
mesh 8	150,000	X

Figure 4.9 shows that poor results were obtained using P1 elements on mesh 3. Further refining the mesh using P1 elements gradually improved the solution as can be seen in figures 4.9, 4.11, 4.13, 4.15, 4.17 and 4.18. P1 elements require far more refinement to obtain a grid-converged solution as can be seen in figures 4.17 and 4.18.

Refinement using P2 elements quickly produces a grid-converged solution. Visually comparing the figures 4.10 and 4.18 shows that P2 elements with 28,000 degrees of freedom yield an equivalent solution to using P1 elements with 150,000 degrees of freedom. This illustrates how using higher order elements will result in less work for an equivalent solution.

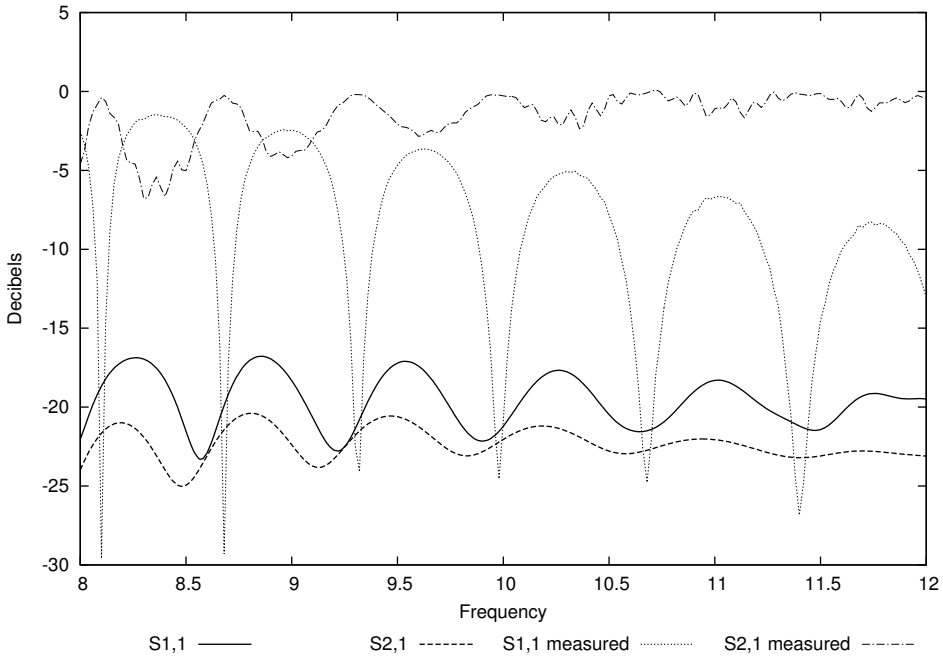

Figure 4.9 Scattering parameters using P1 elements on mesh 3

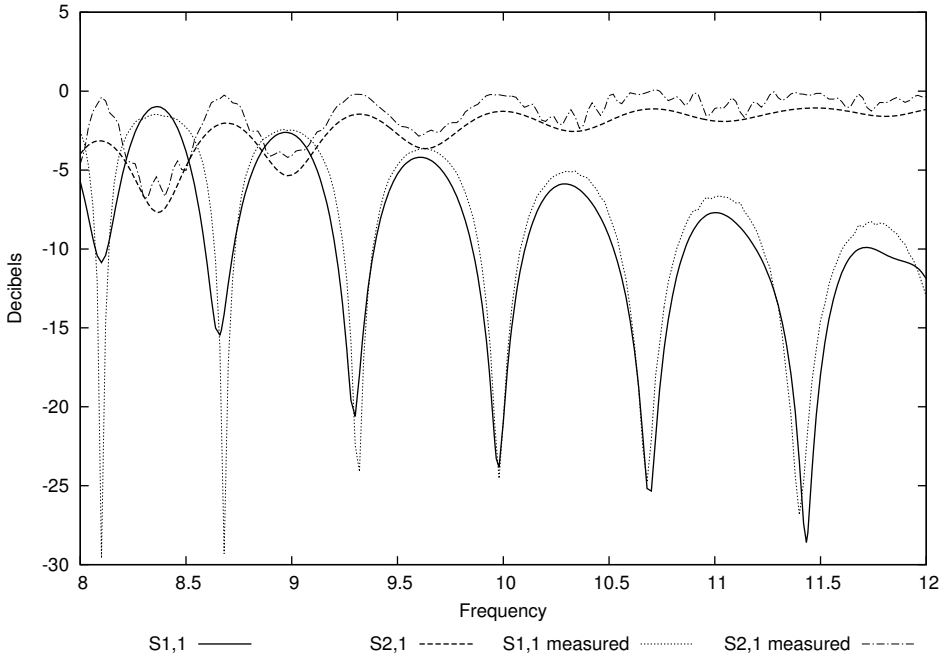

Figure 4.10 Scattering parameters using P2 elements on mesh 3

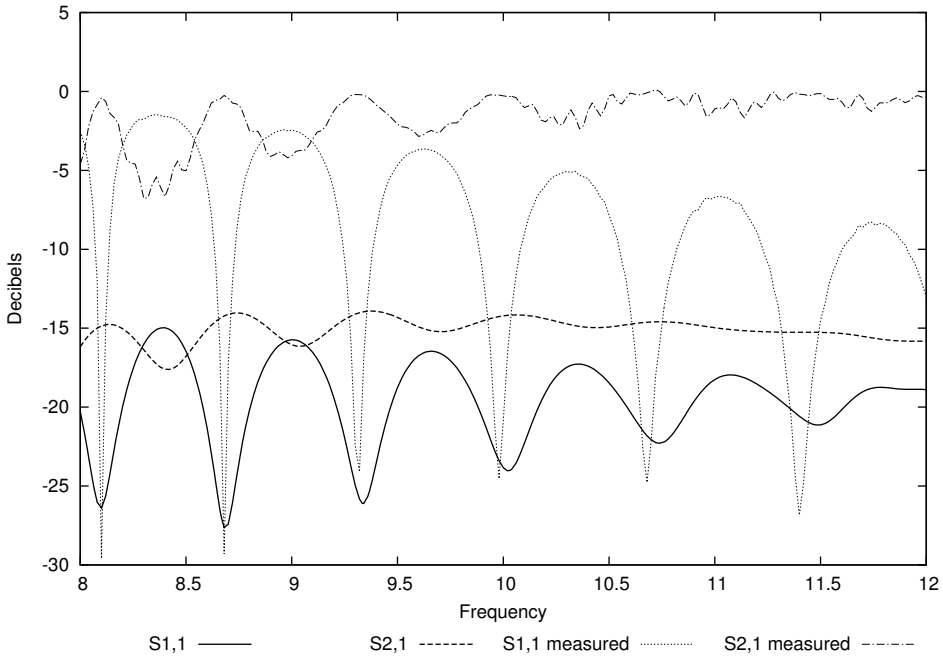

Figure 4.11 Scattering parameters using P1 elements on mesh 4

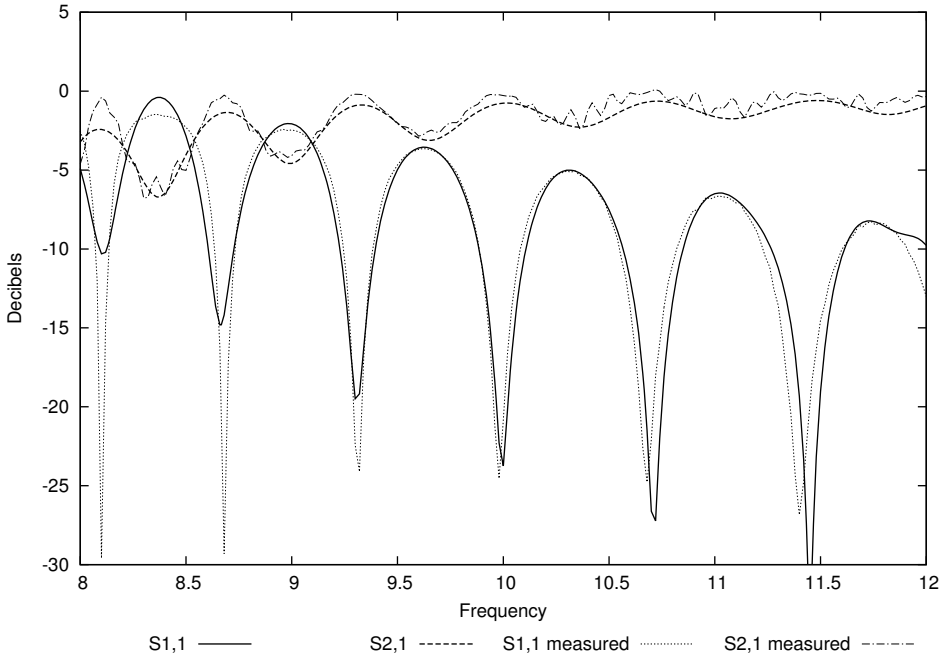

Figure 4.12 Scattering parameters using P2 elements on mesh 4

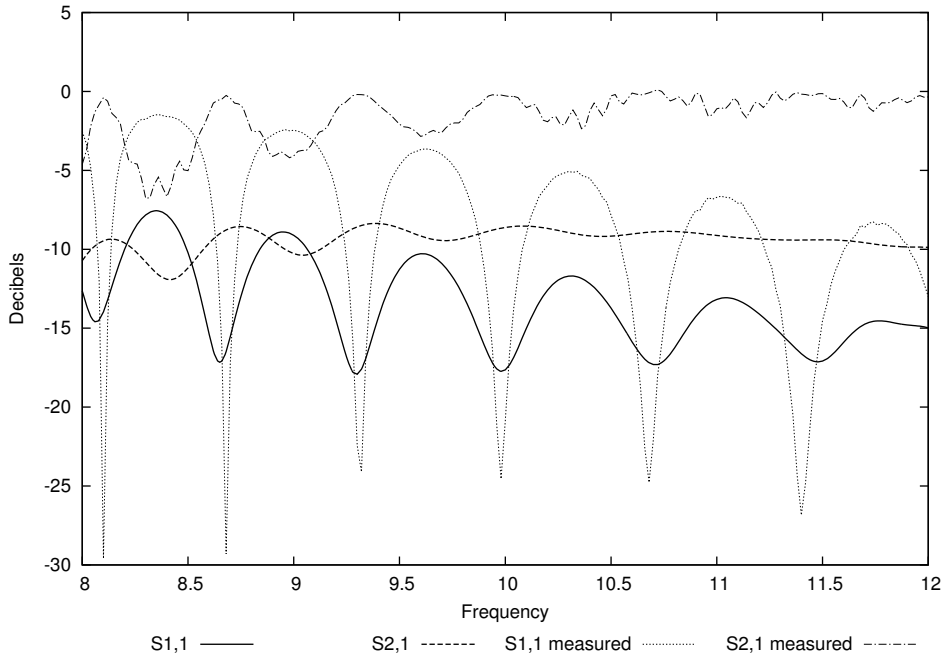

Figure 4.13 Scattering parameters using P1 elements on mesh 5

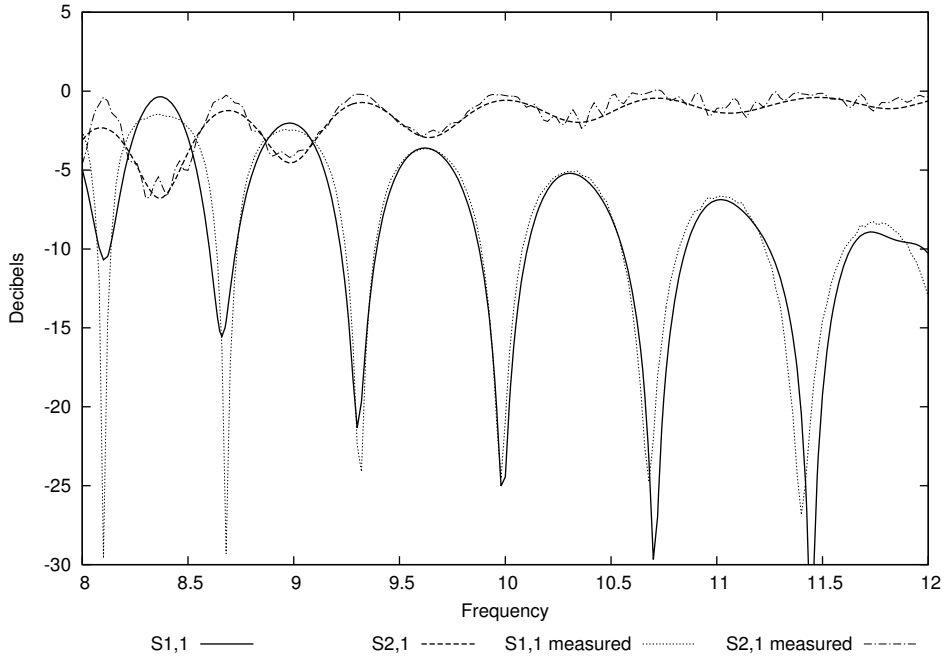

Figure 4.14 Scattering parameters using P2 elements on mesh 5

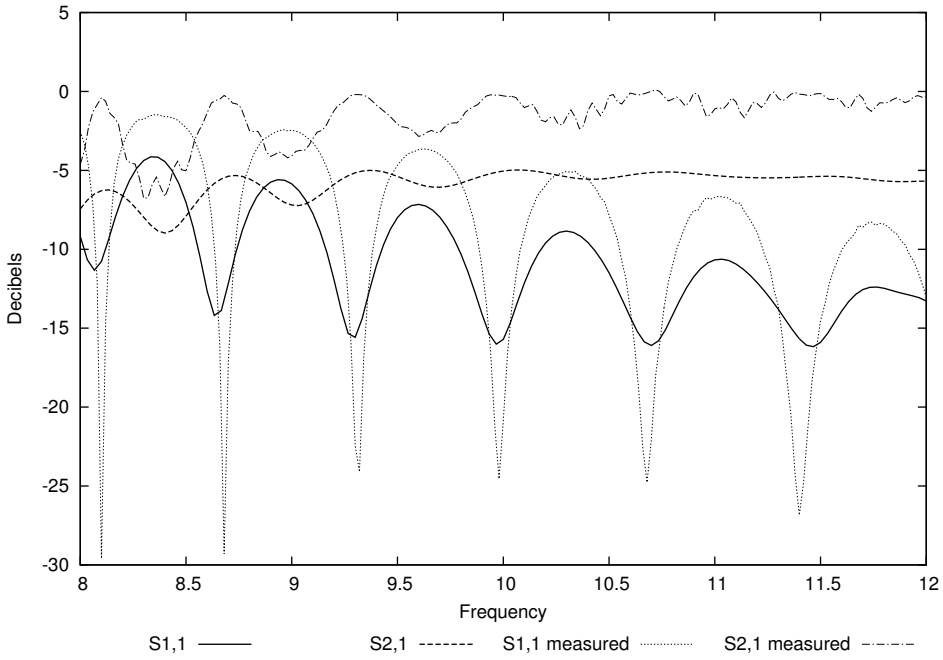

Figure 4.15 Scattering parameters using P1 elements on mesh 6

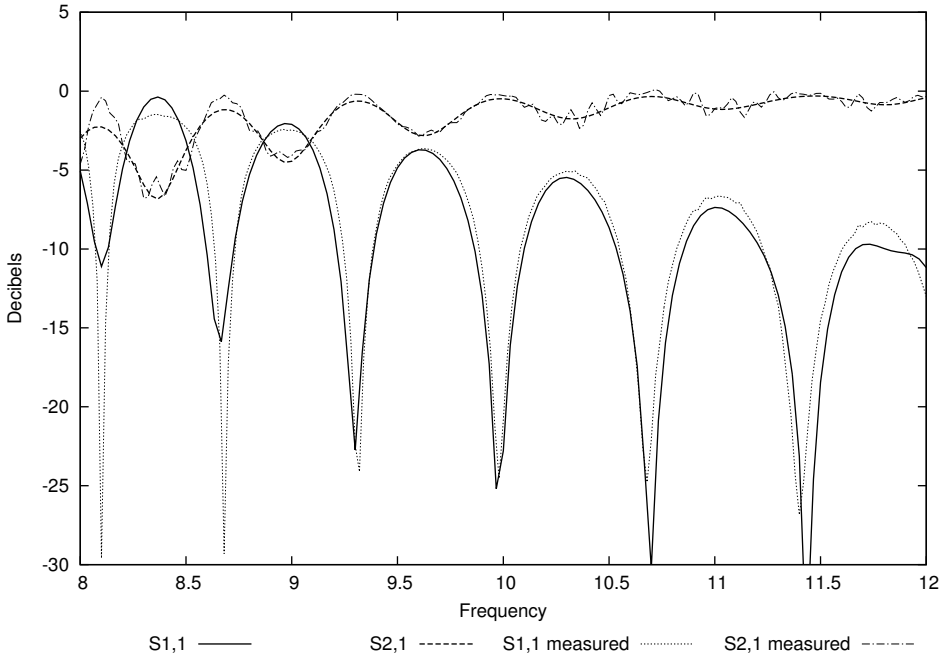

Figure 4.16 Scattering parameters using P2 elements on mesh 6

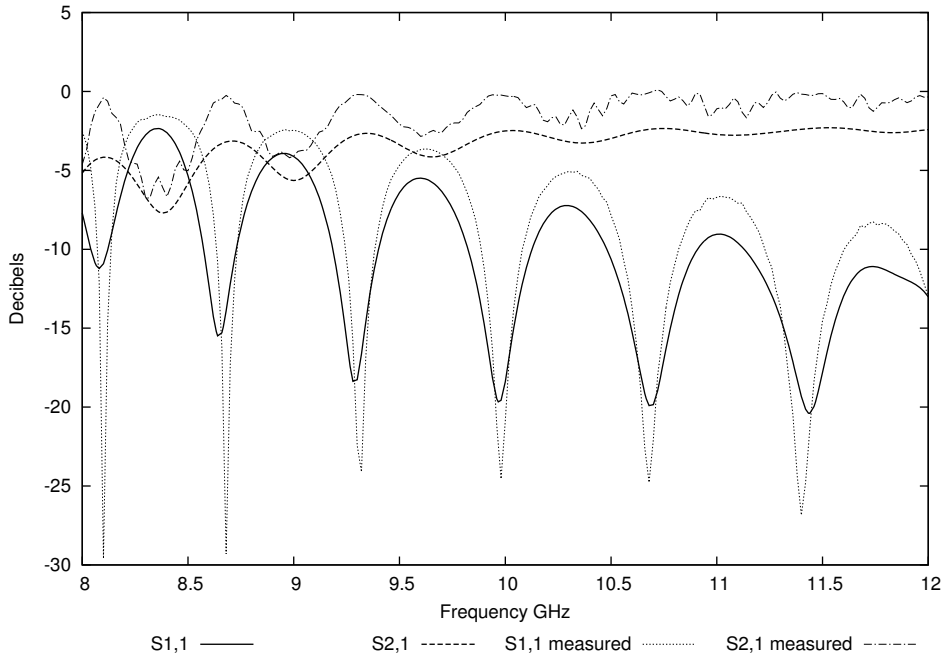

Figure 4.17 Scattering parameters using P1 elements on mesh 7

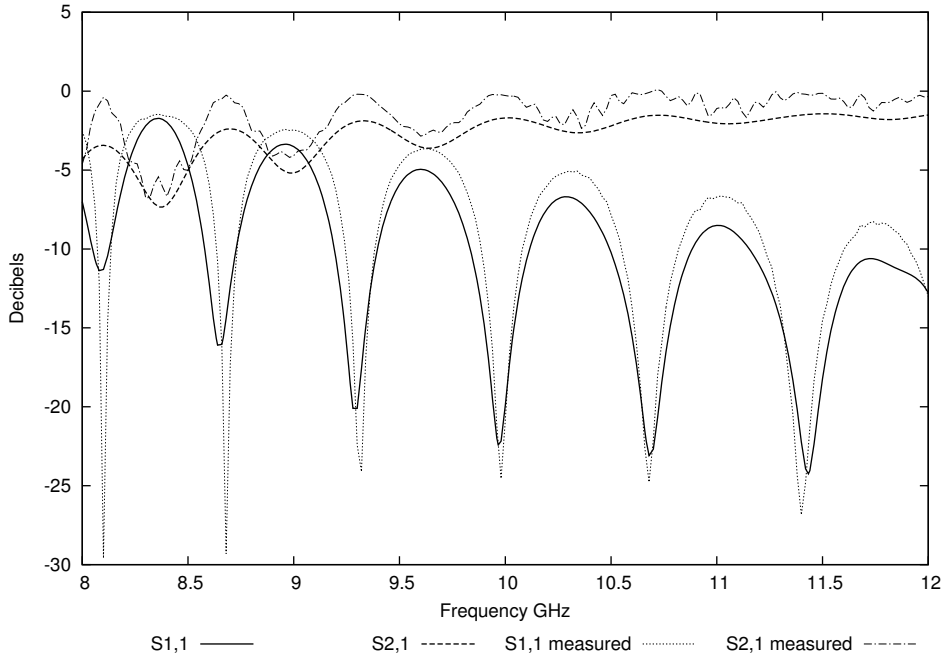

Figure 4.18 scattering parameters using P1 elements on mesh 8

Radar Cross Section of a Sphere

To compute the RCS, the azimuthal angle ϕ was held constant at a value of $\pi/5$ radians from the X-axis. The RCS was then computed at discrete intervals along the sweep of the altitude angle θ from 0 to π, where $\theta = 0$ is the positive Z axis and $\theta = \pi$ is the negative Z axis. As shown in figure 4.19 the incident wave is propagating in the positive Z direction. The analytic solution of the radar cross section of a PEC sphere was also computed at the same intervals.

P-refinement was performed on the radar cross section of a PEC sphere. The P1 mesh consists of 4,428 nodes and the P2 solution computed on the same mesh has 38,284 degrees of freedom. A plane wave enters the mesh traveling in the positive z direction. The Dx field components have been highlighted in Fig. 4.19. The cutaway reveals how the electric field responds when the electromagnetic wave intersects with the sphere.

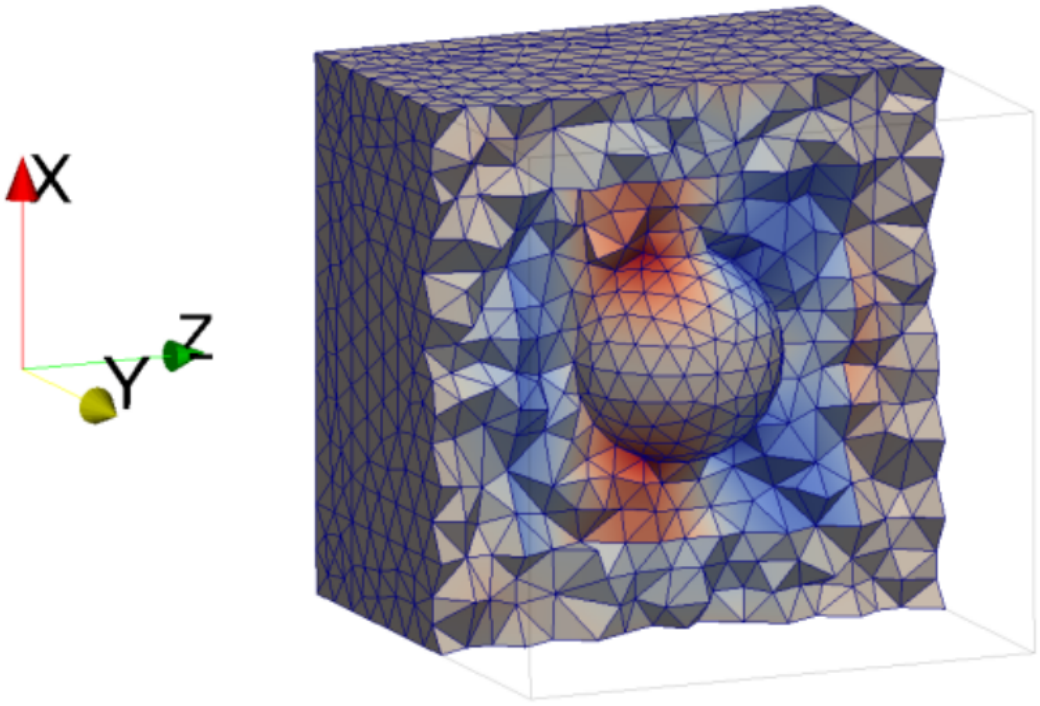

Figure 4.19 Cutaway of the PEC sphere in free space surrounded by PML.

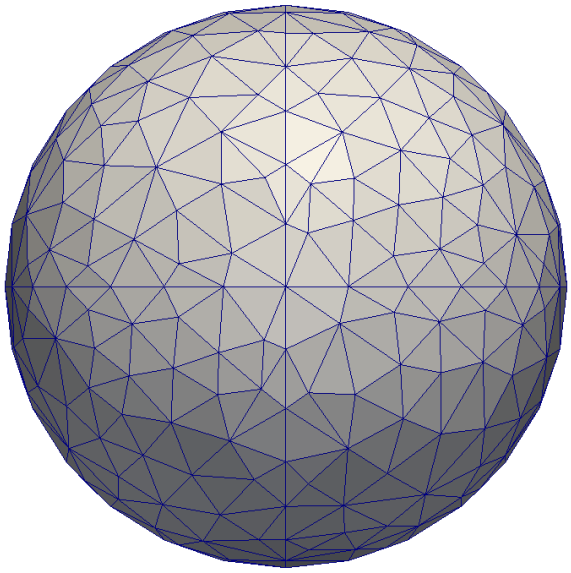

Figure 4.20 Surface of the PEC sphere without projecting the P2 nodes to the surface

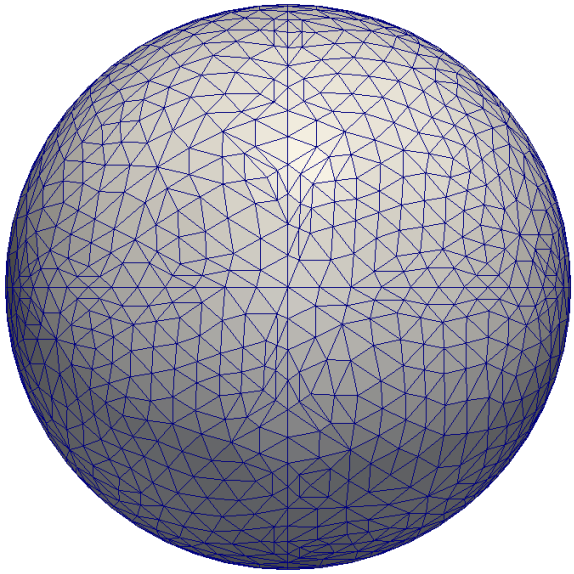

Figure 4.21 Surface of the PEC sphere with the P2 nodes projected onto the surface

Figures 4.20 and 4.21 show the surface connectivity of the PEC sphere. A closer view is shown in figures 4.22 and 4.23. Figure 4.22 shows that using P1 elements produces a linear approximation of a sphere whereas figure 4.23 not only produces a more accurate approximation but the basis functions are also curved, thereby creating a smoother surface.

Results obtained with P1 and P2 elements using a linear approximation of the geometry are shown in figure 4.24. Also shown in the figure are results obtained using properly curved elements to represent the geometry. As seen in figure 4.24 accurately representing the curvature of the surface results in significantly improved results.

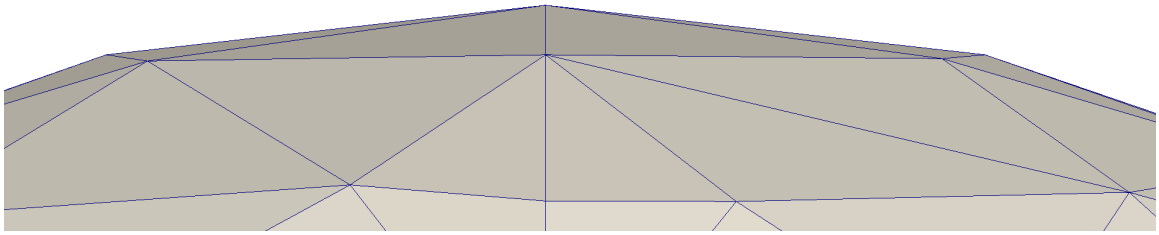

Figure 4.22 Close up view of the surface of the P2 sphere without the higher order nodes projected onto the surface

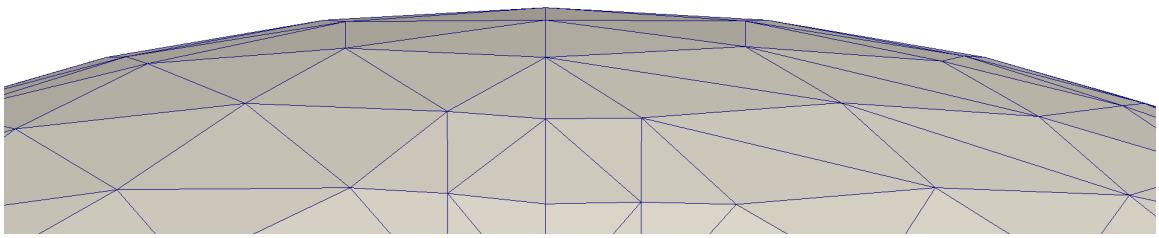

Figure 4.23 Surface of the PEC sphere with the higher order nodes projected onto the surface of the sphere

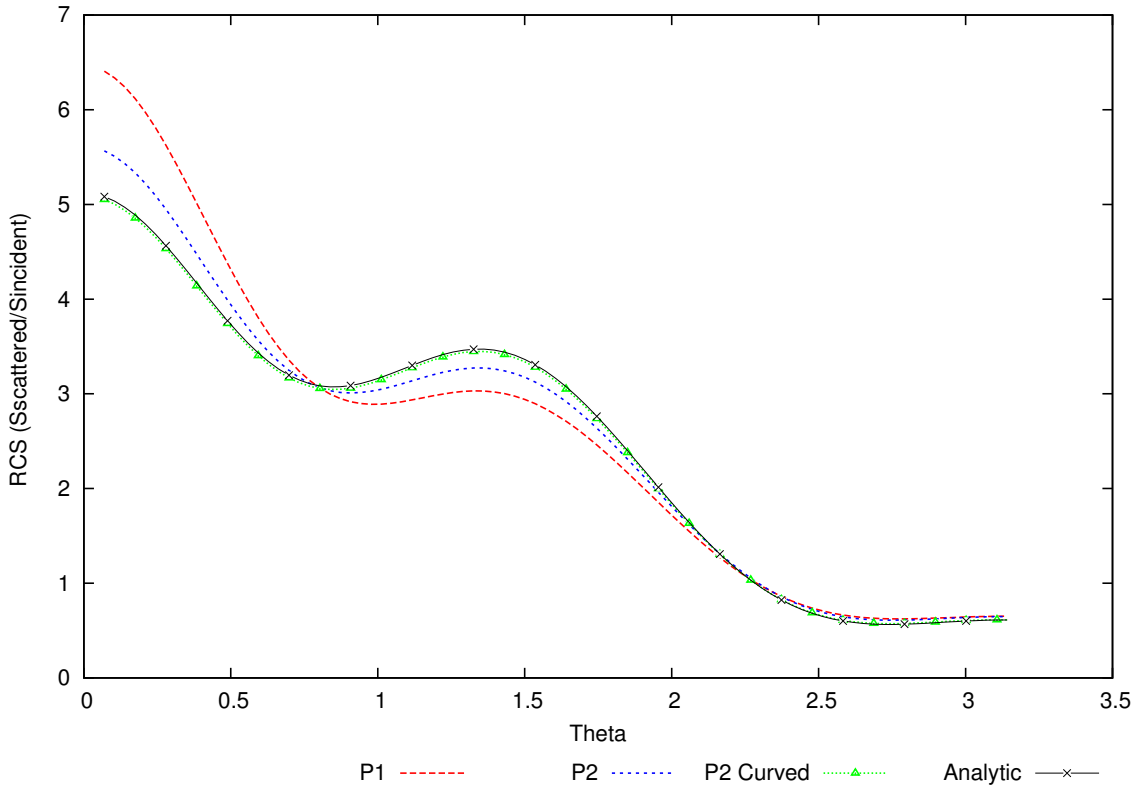

Figure 4.24 P1, P2 and curved P2 solutions for RCS of a sphere

CHAPTER 5

SUMMARY

In summary, four features were successfully added to the solver. The generalization of computing the Fourier transform along each port will assist in analysis of N-port networks. The TE formulation and generalized scattering parameters routine were successfully implemented and verified on the hybrid T-junction. The addition of the Tait-Bryan rotations opens the door to driving ports in arbitrary directions, which greatly improves the applicability of the solver. The grid convergence study performed on the coax-waveguide hybrid circuit illustrates the advantages of using high-order elements and the examination of P-refinement on the radar cross section of a perfect electrically conducting sphere shows that full advantage of the high-order of accuracy is realized only when the curvature of the geometry is accurately represented in the simulation.

REFERENCES

[1] K. S. Yee, "Numerical solution of initial boundary value problems involving Maxwell's equations in isotropic media," Lawrence Radiation Laboratory, Lawrence Radiation Lab., University of California, Livermore, Calif., Tech. Rep., August 1966, under the auspices of the U.S. Atomic Energy commission.

[2] W. K. Anderson, L. Wang, S. Kapadia, C. Tanis, and B. Hilbert, "Petrov-Galerkin and discontinuous-Galerkin methods for time-domain and frequency-domain electromagnetic simulations," *Journal of Computational Physics*, vol. 230, no. 23, pp. 8360–8385, 2011.

[3] P. G. Tait, *An Elementary Treatise on Quaternions.* Cambridge University Press, 1873.

[4] G. T. Ruck, D. E. Barrick, W. D. Stuart, and C. K. Krichbaum, *Radar Cross Section Handbook*, G. T. Ruck, Ed. Plenum Press, 1970.

[5] O. Sergieiev, "Requirements analysis and modelling of an antenna element for breast cancer microwave imaging," Master's thesis, Auckland University of Technology, 2010.

[6] C. A. Balanis, *Advanced Engineering Electromagnetics.* John Wiley & Sons, 1989.

[7] J. N. Reddy, *An Introduction to the Finite Element Method, Third Edition.* McGraw-Hill, 2006.

[8] W. K. Anderson, L. Wang, J. Newman, and S. Kapadia, "Extension of the Petrov-Galerkin time-domain algorithm for dispersive media," *IEEE Microcrowave and Wireless Components Letters*, vol. 23, no. 5, pp. 234–236, May 2013.

[9] F. Assous and E. Sonnendrucker, "Joly-Mercier boundary condition for the finite element solution of 3d maxwell equations," *Mathematical and Computer Modelling*, vol. 51, pp. 935–943, 2010.

[10] A. Oskooi and S. G. Johnson, "Distinguishing correct from incorrect pml proposals and a corrected unsplit pml for anisotropic, dispersive media," *Journal of Computational Physics*, vol. 230, pp. 2369–2377, 2011.

[11] D. M. Pozar, *Microwave Engineering.* John Wiley & Sons, 1998.

[12] F. A. Thomas Sieverding, "Modal analysis of the magic tee," *IEEE Microwvae and Guided Wave Letters*, vol. 3, no. 5, pp. 150–152, May 1993.

[13] R. Glasby and L. Elliot, "Simulation and design of large electromagnetic structures (code-validation experiments)," Final Report Submitted to the University of Tennessee (UTC) SimCenter, 2010 (unpublished).

[14] E. O. Brigham, *The Fast Fourier Transform.* Prentice-Hall, Inc., 1974.

VITA

William Lawton Shoemake was born in Nashville, Tennessee to Jerry and Sandra Shoemake. After graduating Centennial High School in 2006 he attended the University of Tennessee at Chattanooga where he received his bachelors degree in mathematics and physics in 2011. Lawton then accepted a graduate research assistantship at the SimCenter at the University of Tennessee at Chattanooga and completed his masters degree in computational engineering in December 2013.